Improving urban impervious surface extraction by synergizing hyperspectral and polarimetric radar data using sparse representation

Yinyi Lin [a,b], Hongsheng Zhang [a,b,*], Gang Li [c], Luoma Wan [d], Feng Wang [e], Peifeng Ma [f,*], Hui Lin [g]

[a] Department of Geography, The University of Hong Kong, Hong Kong, China
[b] HKU Shenzhen Institute of Research and Innovation, Shenzhen, China
[c] School of Geospatial Engineering and Science, Sun Yat-Sen University, and Southern Marine Science and Engineering Guangdong Laboratory (Zhuhai), Zhuhai, China
[d] Department of Land Surveying and Geo-Informatics, The Hong Kong Polytechnic University, Hong Kong, China
[e] Key Laboratory for Information Science of Electromagnetic Waves (MoE), Fudan University, Shanghai, China
[f] Department of Geography and Resource Management, Institute of Space and Earth Information Science, The Chinese University of Hong Kong, Hong Kong, China
[g] School of Geography and Environment, Jiangxi Normal University, Nanchang, China

ARTICLE INFO

ABSTRACT

Accurate extraction of urban impervious surface (UIS) is essential for urban planning and environmental monitoring. However, multispectral remote sensing data for UIS extraction suffers from the inter-class spectral confusions, e.g. UIS and bare soil, and intra-class variations of sub-class UIS. Hyperspectral and full/dual-polarization synthetic aperture radar (full/dual PolSAR) data provide opportunities for reducing such confusions and have potential for fine UIS mapping, i.e., roads, buildings, and grounds. In this study, we first investigated the hyperspectral data (Gaofen-5) capability to reduce the intra/inter-class misclassification in comparison with multispectral data (Landsat-8). Then, we explored contributions of synergistically using full and dual PolSAR (ALOS-2 and Sentinel-1) with hyperspectral and multispectral data using optical-SAR sparse representation classification (OSSRC). Results showed that both the hyperspectral and the SAR polarization features helped better delineation between UIS and bare soil, and sub-class UIS (roads and buildings). The relative contribution of PolSAR was higher in multispectral data than in hyperspectral data, with full PolSAR contributed significantly. The combined hyperspectral and full PolSAR data using OSSRC delivered the best result, with an overall accuracy higher than 90%. The results indicate the promising capability of synergizing hyperspectral and full/dual PolSAR data for improving UIS extraction from advanced satellite data.

© 2022 National Authority of Remote Sensing & Space Science. Published by Elsevier B.V. This is an open access article under the CC BY-NC-ND license (http://creativecommons.org/licenses/by-nc-nd/4.0/).

1. Introduction

Urban impervious surface (UIS) is related to manmade materials (asphalt, concrete and brick) that are impermeable while the fine UIS is related to sub-types/class UIS, including the roads, buildings and grounds with different social attributes and physical appearance, which demonstrates not only environmental but also social significance (Weng, 2012). Multispectral datasets are efficient for UIS mapping but bare its limitation in inter/intra-class spectral confusion, (UIS and bare soil, asphalt roads and composite tar roofs) (Weng, 2012) and mixed pixels problems. Spectral mixture analysis (Wu and Murray, 2003; Yang and He, 2017) was usually used in medium UIS extraction but usually led to overestimate UIS in low-density urban areas and underestimate them in high-density urban areas. Higher spatial or spectral resolution are potential for sub-class UIS extraction. Pixel-based (Lu and Weng, 2009), object-based (Hu and Weng, 2011), and hybrid methods (Lu et al., 2011) were employed in high-resolution UIS mapping. However, there is tradeoff between spatial and spectral resolution and no single sensor possesses the optimal spatial and spectral resolution (Al-Wassai and Kalyankar, 2013). Hyperspectral data with high spectral dimension shows effectiveness in land cover classification (Xu et al., 2019; Zhang et al., 2019). Hyperion showed better discrimination ability in additional bands in mid-infrared region (Weng et al., 2008), reduce UIS, soil, and vegetation confusion but has limited data coverage (Tang and Xu, 2017). As an emerging hyperspectral satellite, Gaofen-5 (GF-5) (Liu et al., 2019) showed

* Corresponding authors at: Department of Geography, The University of Hong Kong, Hong Kong, China (H. Zhang).

E-mail addresses: yinyilin@hku.hk (Y. Lin), zhanghs@hku.hk (H. Zhang), ligang57@mail.sysu.edu.cn (G. Li), luoma.wan@polyu.edu.hk (L. Wan), fengwang@fudan.edu.cn (F. Wang), mapeifeng@cuhk.edu.hk (P. Ma), huilin@cuhk.edu.hk (H. Lin).

great potential in UIS mapping with spatial resolution of 30 m and 330 spectral bands.

In tropical and subtropical areas, optical datasets suffer contamination from cloudy weather. Synthetic aperture radar (SAR), with all-day and all-weather working capability, can be a great supplement in the cloud-prone tropical and temperate regions (Steinhausen et al., 2018; Mercier et al., 2019; Ling et al., 2021). Multiband, multi-temporal, multi-angle and multi-polarization SAR images (Gamba and Dell'Acqua, 2003; Ratha et al., 2020) were utilized for urban extraction, which demonstrated the feasibility and improvements for human settlement extraction. Polarimetric SAR (PolSAR) (Zhang et al., 2018) and Interferometric SAR (InSAR) (Jiang et al., 2009) were also used for UIS extraction, but the results suffered from vegetation and UIS confusion. The integration of SAR and optical data helped to reduce the confusion between the bright UIS, bare soil and dark UIS (Zhang et al., 2014; Lin et al., 2020). The integration methods for land cover classification usually included the support vector machine (SVM) (Sukawattanavijit et al., 2017), random forests (RF) (Lin et al., 2020), sparse representation-based classification (SRC) (Lin et al., 2019) and deep learning (Zhang et al., 2019), which showed improved performance compared with the single data source. Previous studies also indicated the improvement of inter-class separation using radar and optical data (Sun et al., 2019; Sun et al., 2019; Shao et al., 2016) and sub-class discrimination (Lin et al., 2019). There was also a limitation of scattering confusion between dark UIS and bare soil, and intrinsic shadows and layovers when combining SAR and optical data (Guo et al., 2014).

The integration of hyperspectral and PolSAR data for land cover classification is potential but challenging due to their different imaging geometries and relatively lower data availability. Improved accuracy was shown when combined PolSAR and hyperspectral images (Shokrollahi and Ebadi, 2016; Hu et al., 2019), and few studies were conducted to combine them in the problem of inter/intra-class discrimination. The potential and contribution for higher spectral and polarization characteristics, together with their combination for UIS extraction remain unknown.

In this study, two objectives are to: (1) investigate capability of hyperspectral data in reducing the inter/intra-class confusions; and (2) evaluate the effectiveness and contributions of synergistic use of hyperspectral and PolSAR data for UIS extraction. We developed a methodological framework of jointly using hyperspectral data and SAR data with the proposed Optical-SAR sparse representation-based classification (OSSRC), and compared the results with the state-of-the-art machine learning algorithms. Then we evaluated the contributions of the synergistic use of hyperspectral and PolSAR data compared to multispectral and PolSAR data using the statistical test. This paper is organized as follows: We first introduced the study area and dataset. Then data preprocessing, classification methods, and sample selection and experiment design were explained in the methodology. The results included the spectral analysis of the hyperspectral data, and the accuracy of the UIS extraction results. Finally, we discussed and concluded the performance of hyperspectral and PolSAR data combination for UIS extraction.

2. Study area and dataset

Two study areas include Kwai Tsing (Case 1) in Hong Kong and Lo Wu (Case 2) in Shenzhen (Fig. 1 and Fig. 2). Hong Kong is highly urbanized and the UIS are concentrated and intensive. Kwai Tsing container terminals is the important container logistics processing center, ranking no.8 around the world, which represents coastal area. To the north of Hong Kong, Shenzhen has been rapidly urbanized since 1978 (Yuan et al., 2010). Lo Wu was one of the earliest development zones in Shenzhen, which represents the urbanized area.

The multisource data information is listed in Table 1. GF-5 Advanced Hyperspectral Imager was used with visible and near-infrared reflectance (VNIR) and shortwave infrared reflectance (SWIR). The nearest date cloudless Landsat-8 OLS/TIRS collection 1 level-1 product was used for comparison. The VV and VH dual polarization backscattering coefficient of Sentinel-1 ground range detection level 1 product with IW mode was collected. GF-5, Landsat-8 and Sentinel-1 are within 7-day duration, which ensures better comparison with similar phenological situation, seasonal variety and atmospheric condition. The matching full-polarization ALOS-2 was obtained in 2017 for its low data availability. We assume the land cover changes within 2017 and 2018 are insignificant, which is a simplification for combine different data sources. The L-band ALOS-2/PALSAR stripmap high sensitive mode data was used with HH, HV, VV, VH full-polarimetric mode.

3. Methodology

The overall framework for combining hyperspectral and PolSAR data for impervious surfaces classification is as Fig. 3. The multisource data included hyperspectral data and PolSAR data. After data preprocessing, the hyperspectral data and PolSAR data were registered to generate the multisource data stack. OSSRC was used to fuse and classify the results by constructing the joint optical and SAR dictionary. Three machine learning methods were used for comparison, including the feedforward fully connected neural network (FCNN) (Glorot and Bengio, 2010), RF (Breiman, 2001) and SVM (Cristianini and Shawe-Taylor, 2000). 10-fold cross-validation strategy was used for the results validation and statistical test.

3.1. Preprocessing for multisource data

First, GF-5 was orthorectified using rational polynomial coefficient (RPC) and the DEM of Aster GDEM V2 (Tachikawa et al., 2011) with ground control points' RMSE of 0.5270. Then, we defined the bad bands referring to (Wan et al., 2020): no data in the whole images: SWIR: 43–50, 96–112; strip band with large noise: SWIR: 42, 51–53, 113–115, 171–180. The final bad band is SWIR: 42–53, 96–115, 171–180.

After that, we conducted radiometric calibration, transferred the DN value to radiance in the unit of μW/(cm2 * sr * nm) and ran the fast line-of-sight atmospheric analysis of spectral

Table 1
Data Information of GF-5, Landsat-8 and Sentinel-1.

Sensors		Date	Bands	Wavelength (nm)	Spatial Res (m)
GF-5	VNIR	2018.10.05	150	390-1028	30
	SWIR	2018.10.05	180	1004-2428	
Landsat-8	OLI	2018.10.03	7	443,482.6,561.3,654.6,864.6,1609,2201	30
Sentinel-1	C band	2018.10.09	2	VV and VH	10
ALOS-2	P band	2017.01.11	4	VV, HH, VH, HV	3.21 m/2.86 m

Y. Lin, H. Zhang, G. Li et al.

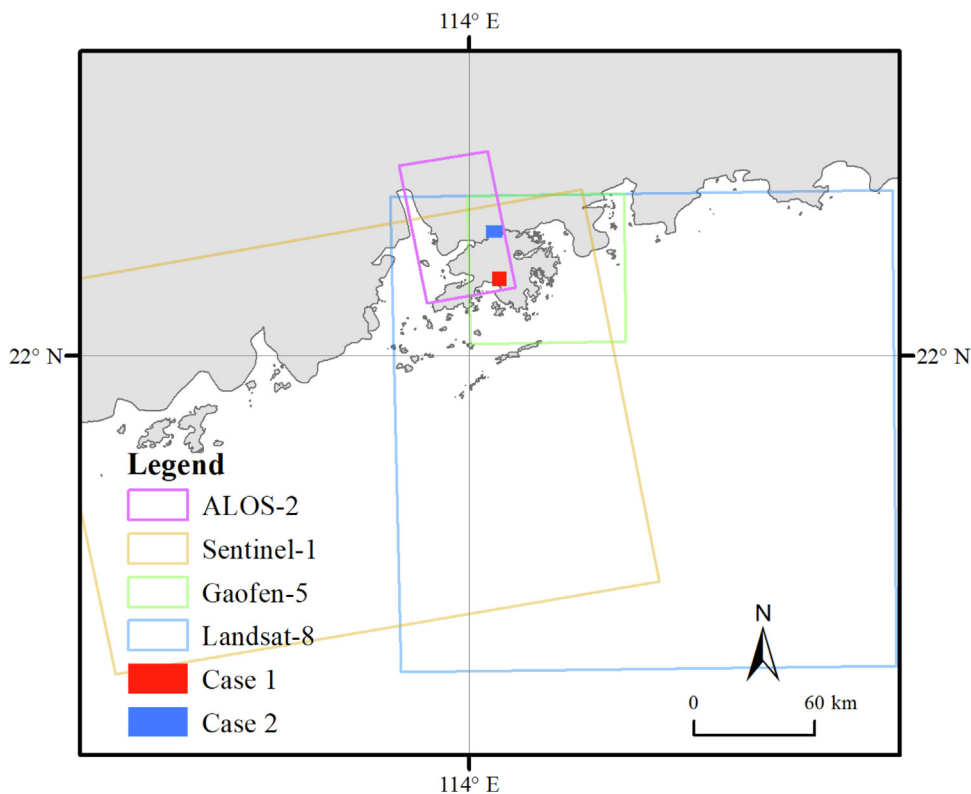Egypt. J. Remote Sensing Space Sci. 25 (2022) 1045–1056

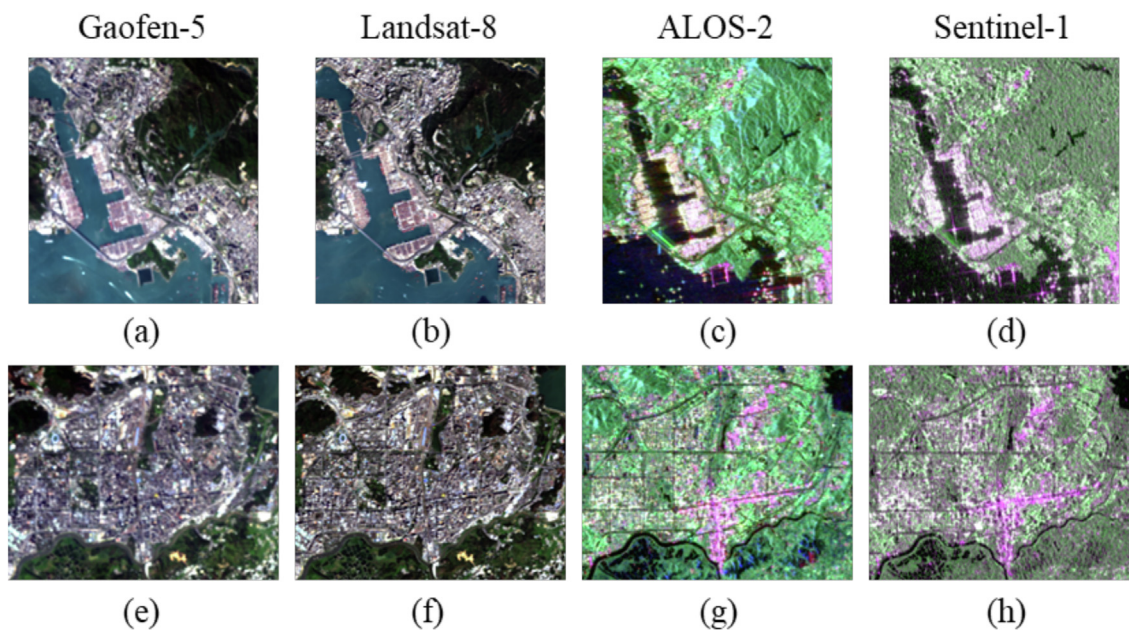**Fig. 1.** Study area and multisource data coverage.

Fig. 2. Study area of Kwai Tsing and Lo Wu. Gaofen-5 RGB composite: 638.3980 nm, 548.4660 nm, 471.4250 nm. Landsat-8: 654.6 nm, 561.3 nm, 482.6 nm. ALOS-2: T22, T33, T11 coherence matrix. Sentinel-1: VH, VV, VH terrain-flattened gamma naught.

hypercubes (FLAASH) (Abreu & Anderson, 1996) using the ENVI 5.3. We used the tropical atmospheric model and 1135 nm for Water Absorption Feature and urban aerosol model. Landsat-8 used the same parameters as GF-5 to get the surface reflectance, ensuring similar atmospheric setting.

Sentinel-1 was preprocessed using the Sentinel Toolbox (Veci et al., 2014): apply orbit file, thermal noise removal, radiometric calibration, radiometric terrain flattening (reducing the terrain effects of the mountain) and terrain correction. Sentinel-1 terrain-flattened gamma naught γ^o of VV and VH were used (Small, 2011). ALOS-2 conducted the radiometric calibration, box car filter to generate the T coherence matrix, and terrain correction. The T matrix is diagonal symmetry matrix as equation (1), including T_{11}, T_{12}, T_{13}, T_{22}, T_{23} and T_{33}.

Y. Lin, H. Zhang, G. Li et al.

Egypt. J. Remote Sensing Space Sci. 25 (2022) 1045–1056

Multisource Data

Data Preprocessing

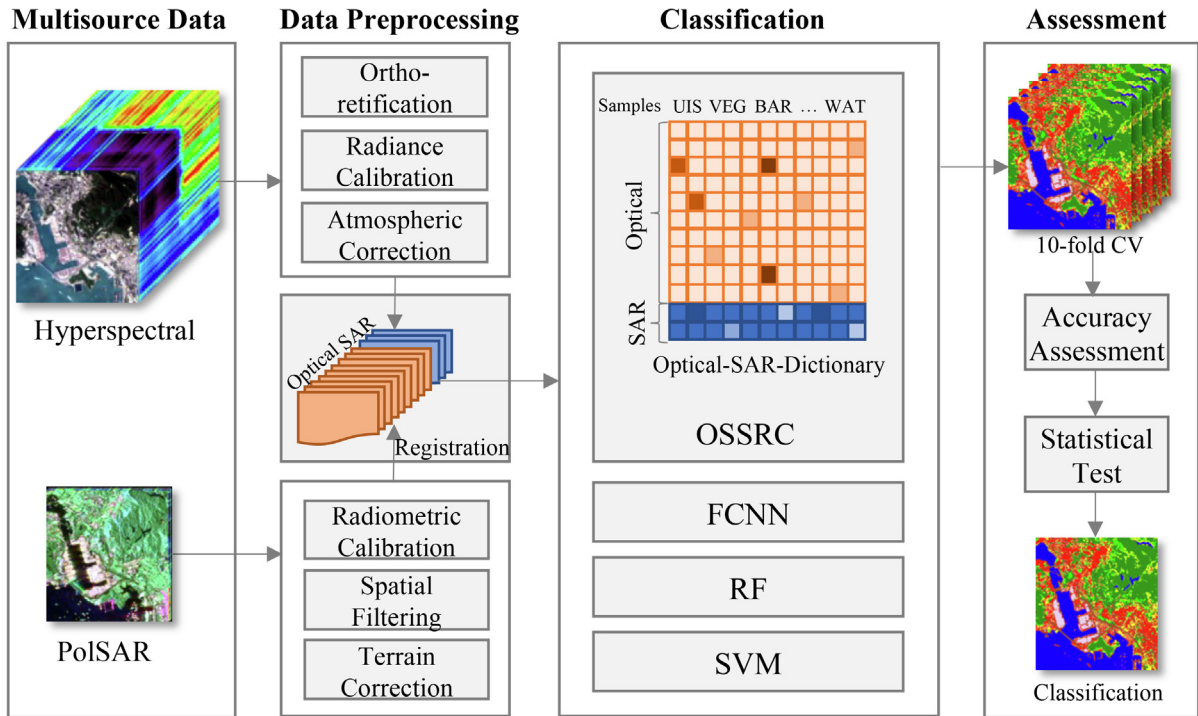## Classification

Assessment

Fig. 3. Flowchart of synergizing hyperspectral and PolSAR data for UIS extraction.

$$T = \begin{bmatrix} T_{11} & T_{12} & T_{13} \\ T_{21} & T_{22} & T_{23} \\ T_{31} & T_{32} & T_{33} \end{bmatrix} \tag{1}$$

Landsat-8 worked as the base map for its well georegistration. GF-5, Sentinel-1 and ALOS-2 were registered to Landsat-8, resampled using the bilinear interpolation with resolution of 30 m, under the projected coordinate of WGS 84, UTM 50N for the later classification process.

3.2. Optical-SAR sparse representation for UIS extraction

Optical-SAR sparse representation-based classification (OSSRC) modified from SRC (Wright et al., 2009; Mairal et al., 2014) was used for the pixel-based UIS extraction, which was chosen to test its ability to extract sub-type UIS. Though mixed pixels exist, the morphological features can help to determine the sub-type UIS (Weng, 2012). Hyperspectral and polarization features give higher opportunity for fine UIS discrimination. Assuming that machine learning algorithms can handle the high dimension features, feature selection is not included in this study. The classification process combined optical and SAR data at the feature level (Zhang and Ru, 2018). The classifiers learned from the concatenated optical and SAR features at the pixel dimension and compared the performance with using single optical features alone. SRC has been usually combined with other components for image classification, for example, multiple ensembles (Cao et al., 2016) or multi-temporal features (Li et al., 2016), while the joint optical and SAR multisource dictionary was used in this study. OSSRC supposed the training samples are overcomplete and well represents the study area, then the testing samples can be linearly represented by the training samples. Supposed there are C class, a total of $n = \sum_i^C n_i, i = 1, 2, \cdots, C$ samples. The optical and SAR training samples are combined together to build a joint two-dimensional optical and SAR dictionary X as in equation (2), one dimension rep-

resents the multisource data while the other dimension represents the multiclass samples.

$$X = \begin{bmatrix} X_{Optical} \\ (X_{SAR}) \end{bmatrix} = [x_1, x_2, \cdots, x_C] \in \mathbb{R}^{m \times n} \tag{2}$$

$X_{Optical}$ indicates the hyperspectral/multispectral features. X_{SAR} denotes dual/full PolSAR. So the testing samples y can be represented as,

$$y = X\alpha + n \tag{3}$$

where n is the noise. We used l_1 norm to solve the situation with the least angle regression algorithms (Efron et al., 2004), so the coefficient α can be calculated as,

$$\hat{\alpha} = \arg\min\|y - X\alpha\|_2^2 + \lambda\|\alpha\|_1 \text{s.t.} \|\alpha\|_1 \le \lambda \tag{4}$$

λ is 0.15 in this study, which limits the number of non-zeros coefficients. With the sparse coefficient α, the label of the class can be computed by the largest response (largest coefficient) of the corresponding class as in equation (5), which is a simplification for the minimum residuals in (Lin et al., 2019) and requires less computation time:

$$\text{class}(y) = \arg\max_{c=1,2,\cdots,C} \alpha_c \tag{5}$$

SVM (Cristianini and Shawe-Taylor, 2000), RF (Breiman, 2001) and FCNN (Glorot and Bengio, 2010; He et al., 2015) were used for comparison. RF is an ensemble method that uses the bootstrap aggregation (bagging) to build decision trees from the concatenated optical and SAR features for classification and 200 trees are used in this study. SVM creates a hyperplane to separate the concatenated optical and SAR features into different classes. The FCNN is constructed with a fully connected layer to learn the concatenated optical and SAR features, followed by a ReLU activation func-

Y. Lin, H. Zhang, G. Li et al.

Egypt. J. Remote Sensing Space Sci. 25 (2022) 1045–1056

tion, a fully connected layer and a Softmax function for classification. The classification processes were conducted on Matlab 2021b.

3.3. Sample selection scheme and experimental design

Cluster sampling schema (McCoy, 2005) were used to collect homogeneous and contiguous samples referring to the high-resolution google earth images. A two-level class scheme was chosen: vegetation: vegetation (VEG) and grassland (GRASS); UIS: building (BUL), road (ROAD), ground (GROUND), other UIS (OTHER); bare land (BAR); and water: water (WAT) and pond (POND). Kwai Tsing contains a total of 2422 samples, with 330 BAR, 442 BUL, 224 GRASS, 201 GROUND, 203 OTHERS, 527 ROADS, 244 VEG and 251 WAT. The containers samples of Kwai Tsing container terminals were chosen for it demonstrated different social and physical properties. Lo Wu had the additional 217 PONDS, together with 357 BAR, 492 BUL, 276 GRASS, 251 GROUND, 476 ROAD, 247 VEG and 253 WAT, altogether 2569 samples.

The datasets were divided into 6 groups to: explore the effectiveness of optical data (multispectral and hyperspectral data alone) for UIS extraction, and explore the effectiveness of combining optical (multispectral and hyperspectral data) and PolSAR (dual and full PolSAR) for UIS extraction, i.e., (1) Landsat 8 alone (g-L8; 2) GF-5 alone (g-GF5; 3) Landsat 8 and Sentinel-1 (g-L8-S1; 4) GF-5 and Sentinel-1 (g-GF5-S1; 5) Landsat 8 and ALOS-2 (g-L8-ALOS2; 6) GF-5 and ALOS-2 (g-GF5-ALOS2). Confusion matrix, overall accuracy and kappa coefficient (Fitzgerald and Lees, 1994) were calculated for accuracy analysis.

We designed the experiment to test whether classification result of hyperspectral features was better than multispectral features and how much contributions of PolSAR were. 10-fold cross validation together with nonparametric Friedman test (Demsar, 2006) were used to evaluate the result. The groups worked as the treatment factors while the study cases and the classifiers were the blocking factors. The classification accuracy worked as the repeated observation. Under the null hypothesis, it supposed that the comparative treatments (6 groups) are equivalent so their accuracy ranks are also equal. Supposed that there are $i = 1, \cdots, k$ algorithms on $j = 1, \ldots, N$ data sets, r_i^j represents the rank of i algorithm on j data set, $R_j = \frac{1}{N}\sum_j r_{i\cdot}^j$. The Freidman statistics obeys the χ_F^2 distribution with k-1 freedom.

$$\chi_F^2 = \frac{12N}{k(k+1)}\left[\sum_j R_j^2 - \frac{k(k+1)^2}{4}\right] \tag{6}$$

If the null hypothesis is rejected, the post-hoc test will further process. Tukey test (Hochberg and Tamhane., 1987) is used and two groups are significantly different from each other when the corresponding average differs.

4. Results

4.1. Spectral analysis of GF-5 and Landsat-8

4.1.1. Spectral characteristics of optical data

The spectrum of GF-5 was consecutive covering from 390 nm to 2428 nm (Fig. 4). Landsat-8 was coarse, separated, and in different intervals (Fig. 4 bold black line). The spectrum of GF-5 and Landsat-8 showed similar trend in different classes. The surface reflectance of Landsat-8 was lower than the GF-5, but it had variance in different bands and classes. The spectral characteristics of BUL, ROAD, GROUND were very similar in both GF-5 and Landsat-8. Actually, the materials of these three sub-class UIS were usually asphalt and cement, showing similarities in the whole spectrum. The spec-

trum of BAR was similar with BUL, ROAD, GROUND and OTHER in VNIR, while in SWIR, it was more similar with GROUND. BAR showed high reflectance from 730 nm to 1300 nm. In this respect, the misclassification between BAR and UIS was not as significant as in the sub-class UIS, i.e., BUL and ROAD. In addition, GF-5 showed its great potential in sub-class discrimination, i.e., VEG and GRASS, WAT and POND.

4.1.2. Spectral comparison between hyperspectral and multispectral features

Consistent centre wavelength of reflectance of GF-5 and Landsat-8 were compared (Table 2 and Fig. 5). Overall, the consistency between GF-5 and Landsat-8 was 0.9316, with R-squared of 0.9590. The two sensors worked in 2-day gap, which reduced the phenological variance. The variance came from the sensor characteristics and flight time. The flight time of Landsat-8 was GMT 2:46:5 while GF-5 was GMT 5:40:38, which had three hours lag between morning and mid-afternoon. It was reasonable that the light was more intensive in mid-afternoon in GF-5. When it comes to the class-specific consistency, it showed that the two datasets were consistent in BAR, VEG, GRASS, WAT and POND, with R-square higher than 0.9. Whereas, variance shown in the sub-class UIS including BUL, ROAD, and GROUND. In medium resolution dataset, the mixed pixel problem existed between sub-class UIS, which led to the diversity and inconsistency between two datasets. As mentioned above, the sub-class UIS confusion may be higher than the UIS-bare land confusion.

4.2. Accuracy of UIS extraction

4.2.1. Accuracy assessment of UIS extraction using different machine learning methods

The 10-fold cross validation averaged classification results were shown in Fig. 6 and in Table 3. Both the OSSRC and the FCNN showed higher accuracy, followed by RF, and SVM, but FCNN required a much longer computation time. Generally, different classifiers all performed the best in the GF-5 groups, i.e., g-GF5-ALOS2, g-GF5-S1, and g-GF5. In Case 1, OSSRC and FCNN outperformed in road extraction, but FCNN had some false alarms in the bare land in the mountains (Fig. 7). RF and SVM tended to misclassify the BAR as ROAD. For Case 2, OSSRC and FCNN had good performance in the intra-class discrimination of WAT and POND while RF and SVM doesn't. But FCNN did not keep the good shape in the river classification.

4.2.2. Improvements of UIS extraction from hyperspectral and polarimetric features

Overall, g-GF5-ALOS2 using OSSRC obtained the highest overall accuracy and kappa coefficient, followed by g-GF5-S1, g-GF5, g-L8-ALOS2, g-L8-S1, and g-L8. g-L8 classification results had more noises than the other groups (Fig. 8). SAR backscattering coefficient greatly reduced the noise. The containers were near the pier, which were made of aluminum alloy, steel and etc., showing diverse reflection. Dense urbanized area contains large portions of mixed pixels with spectral and double bounce mixing (Fig. 9). The spectral confusions can be significantly reduced when SAR is added.

The road pattern was discriminated more clearly in g-GF5-S1 and g-GF5-ALOS2 (Fig. 10). The third row shows bare land discrimination has greatly improved with hyperspectral features. Quantitative analysis of case 1 was conducted (Table 4 and Table 5). g-L8 showed that 26 BUL were misclassified as BAR. Sub-class UIS analysis showed 62, 26, 11 BUL were misclassified with ROAD, GROUND, and OTHER respectively. With Sentinel-1/ALOS-2 supplement, the BUL to BAR misclassification reduced to 21/17. The sub-class UIS misclassifications of ROAD, GROUND, and OTHER were declined to 33, 21, 6 respectively when ALOS-2 integrated.

Y. Lin, H. Zhang, G. Li et al.

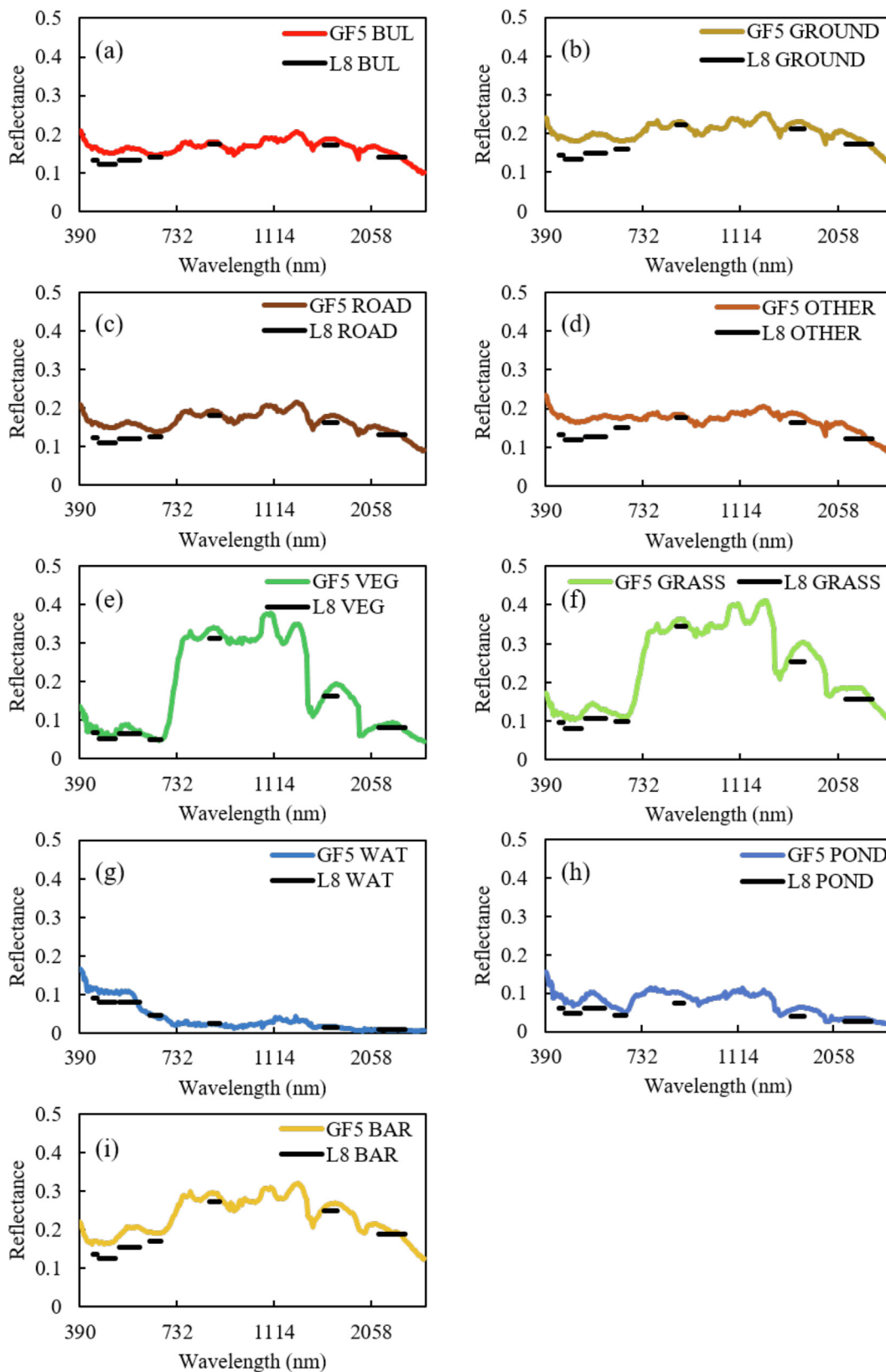Egypt. J. Remote Sensing Space Sci. 25 (2022) 1045–1056

Fig. 4. Surface reflectance of GF-5 and Landsat-8.

Table 2
Class-specific relationship between GF-5 and Landsat-8.

R^2	BAR	BUL	GROUND	ROAD	OTHER	GRASS	VEG	WAT	POND	All
GF5-L8	0.9345	0.6264	0.7530	0.6250	0.3829	0.9892	0.9957	0.9802	0.9154	0.9573

Y. Lin, H. Zhang, G. Li et al.

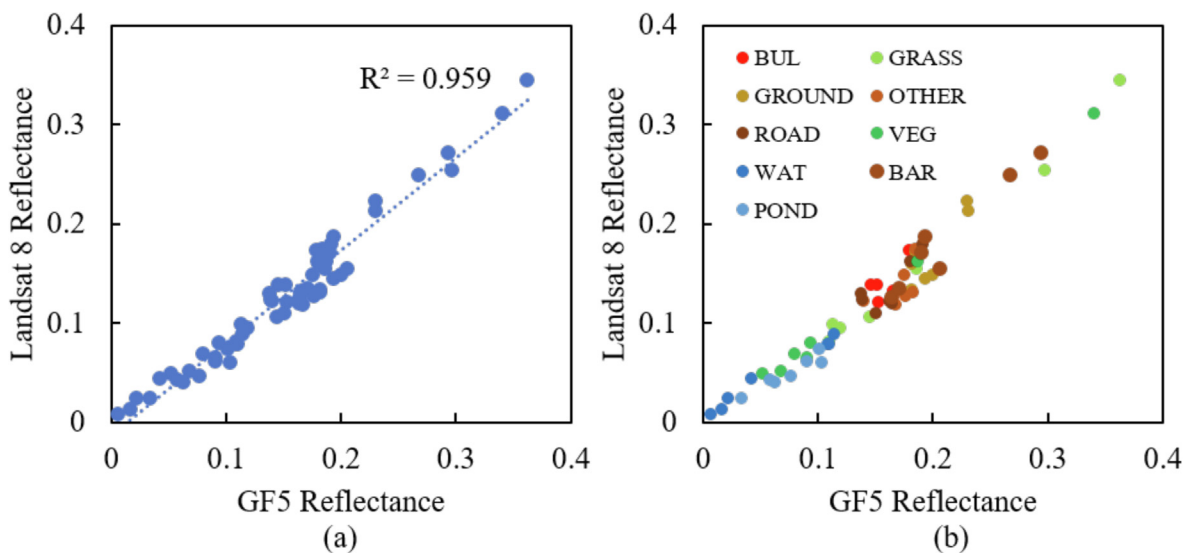*Egypt. J. Remote Sensing Space Sci. 25 (2022) 1045–1056*

Fig. 5. Surface reflectance relationship between GF-5 and Landsat-8. (a) All class; (b) Per class.
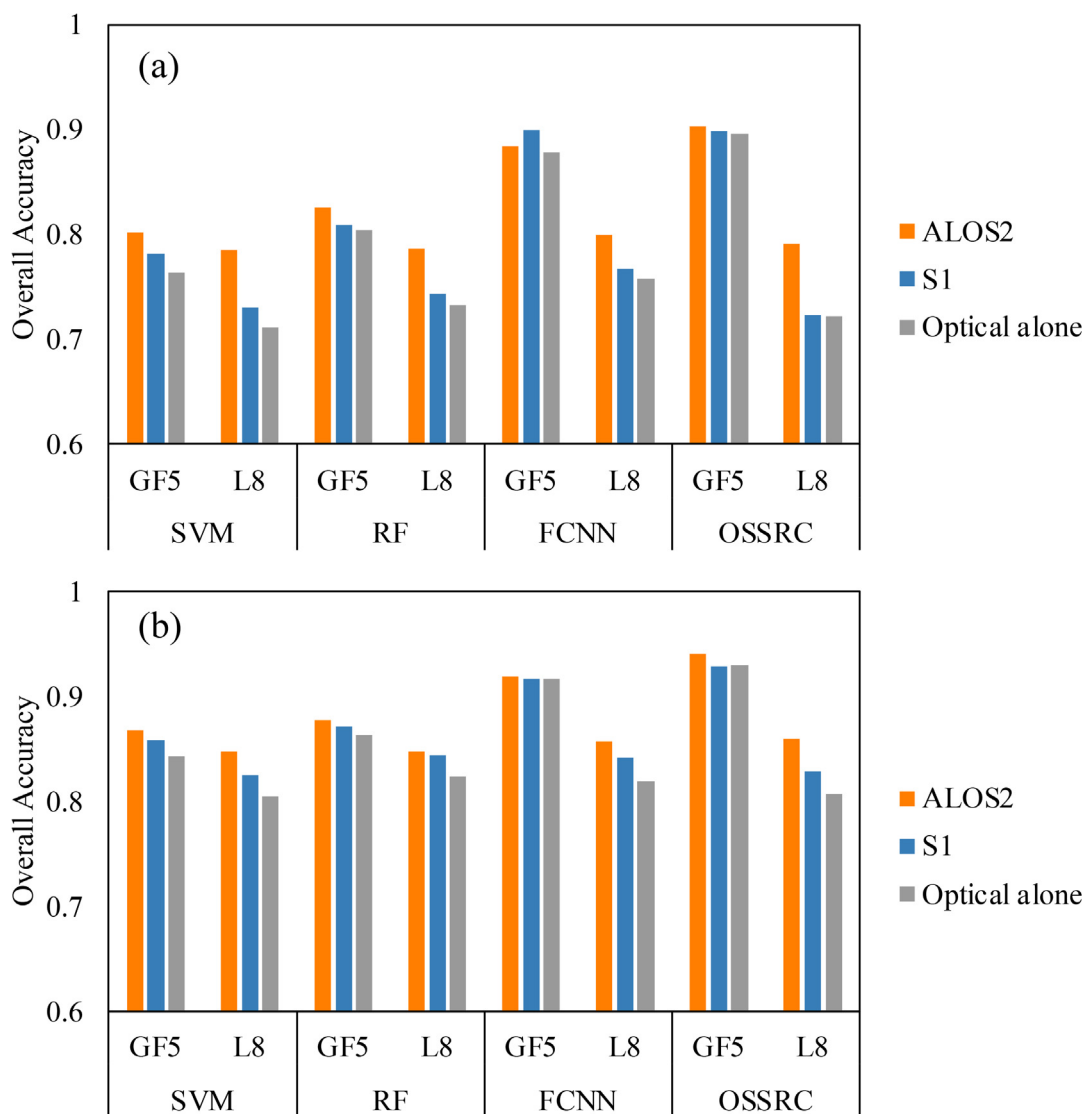
Fig. 6. Mean overall accuracy using different data groups. (a): Case 1, (b): Case 2.

Y. Lin, H. Zhang, G. Li et al.

Egypt. J. Remote Sensing Space Sci. 25 (2022) 1045–1056

Table 3

Averaged classification results of different classifiers.

|	Group	SVM		RF		FCNN		OSSRC	
		OA (%)	Kappa	OA (%)	Kappa	OA (%)	Kappa	OA (%)	Kappa
Case 1	GF-5	76.43	0.7225	80.38	0.7702	87.81	0.8576	89.64	0.8793
	GF5-S1	78.11	0.7429	80.92	0.7765	89.97	0.8828	89.80	0.8811
	GF5-ALOS2	80.14	0.7669	82.57	0.7958	88.40	0.8645	**90.30**	**0.8870**
	L8	71.14	0.6606	73.33	0.6880	75.81	0.7169	72.17	0.6761
	L8-S1	72.99	0.6837	74.36	0.6999	76.72	0.7279	72.34	0.6778
	L8-ALOS2	78.53	0.7490	78.70	0.7509	79.94	0.7659	79.15	0.7571
Case 2	GF-5	84.31	0.8178	86.30	0.8409	91.67	0.9023	92.99	0.9187
	GF5-S1	85.87	0.8358	87.23	0.8518	91.66	0.9020	92.95	0.9182
	GF5-ALOS2	86.76	0.8462	87.74	0.8576	91.99	0.9060	**94.12**	**0.9318**
	L8	80.49	0.7733	82.40	0.7956	81.91	0.7873	80.69	0.7761
	L8-S1	82.48	0.7962	84.47	0.8196	84.14	0.8136	82.83	0.8008
	L8-ALOS2	84.81	0.8233	84.81	0.8233	85.75	0.8328	85.99	0.8374
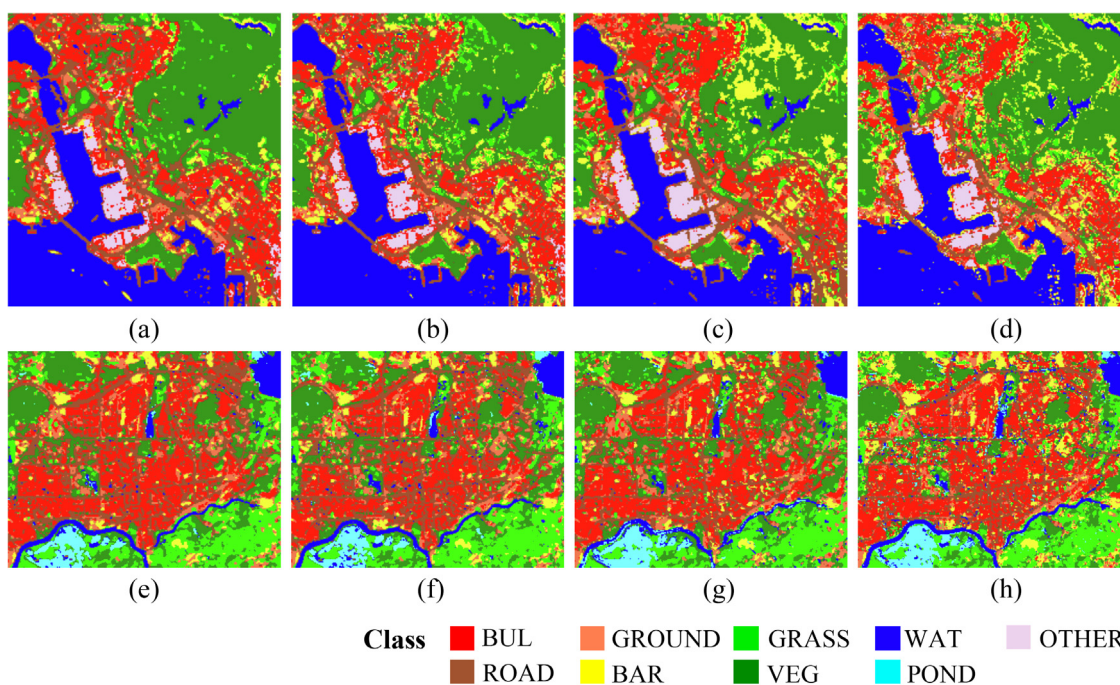
Fig. 7. Classification results of different classifiers in two cases (Case 1: a-d; Case 2: e-h). (a&e). SVM, (b&f). RF, (e&g). FCNN, (d&h). OSSRC.

But Sentinel-1 cannot contribute much to the results. Comparing to g-L8, the hyperspectral features of g-GF5 also improved the mis-classification in g-L8-S1. When both features were used, in g-GF5-S1/GF5-ALOS2, major improvements came in the sub-class UIS discrimination, the BUL to ROAD, GROUND, and OTHER mis-classification were reduced to 22/19, 10/6, 3/1. The combination of hyperspectral features and full PolSAR demonstrated the best results, yielding overall accuracy higher than 90%.

4.2.3. Friedman significant test

Pair-wise Friedman test calculated the p-value of different groups (Table 6). The classification result of hyperspectral data was significantly different from multispectral data with p-value smaller than 0.001. In addition, the contribution of dual and full PolSAR in multispectral data was significant with p-value smaller than 0.001. Whereas, the contribution of SAR in hyperspectral data was not so significant as in multispectral data. Still, we can observe full PolSAR significantly improve the GF-5 while the dual PolSAR doesn't. The average accuracy improvement in g-GF5-S1 is slight comparing with g-GF5.

5. Discussion

The sub-class UIS in urban environment are diverse and complicated, showing different material, conductivity and shape. This study categorized the sub-class UIS into roads, buildings, grounds, and other UIS according to their social attributes and physical morphology. The sub-class UIS reflection in different data sets are different. The BIS and DIS in optical datasets may not correspond to "bright" or "dark" SAR datasets. As a result, the social entity of categorization of sub-class UIS is a better choice for multi-modality UIS mapping.

The hyperspectral and PolSAR data showed the capability for pixel-level sub-class UIS mapping. The inter-class confusion of bare land and UIS was not the major problem, instead, sub-class UIS confusion came to the front. The hyperspectral improvements lied in the extended spectrum, for example, the bare soil was similar with buildings, roads, grounds in VNIR, while in SWIR, it was similar with grounds. Sub-class UIS classification was trivial in medium resolution data mapping, not only for the mixed pixels problem, but also the similar materials of different sub-class UIS.
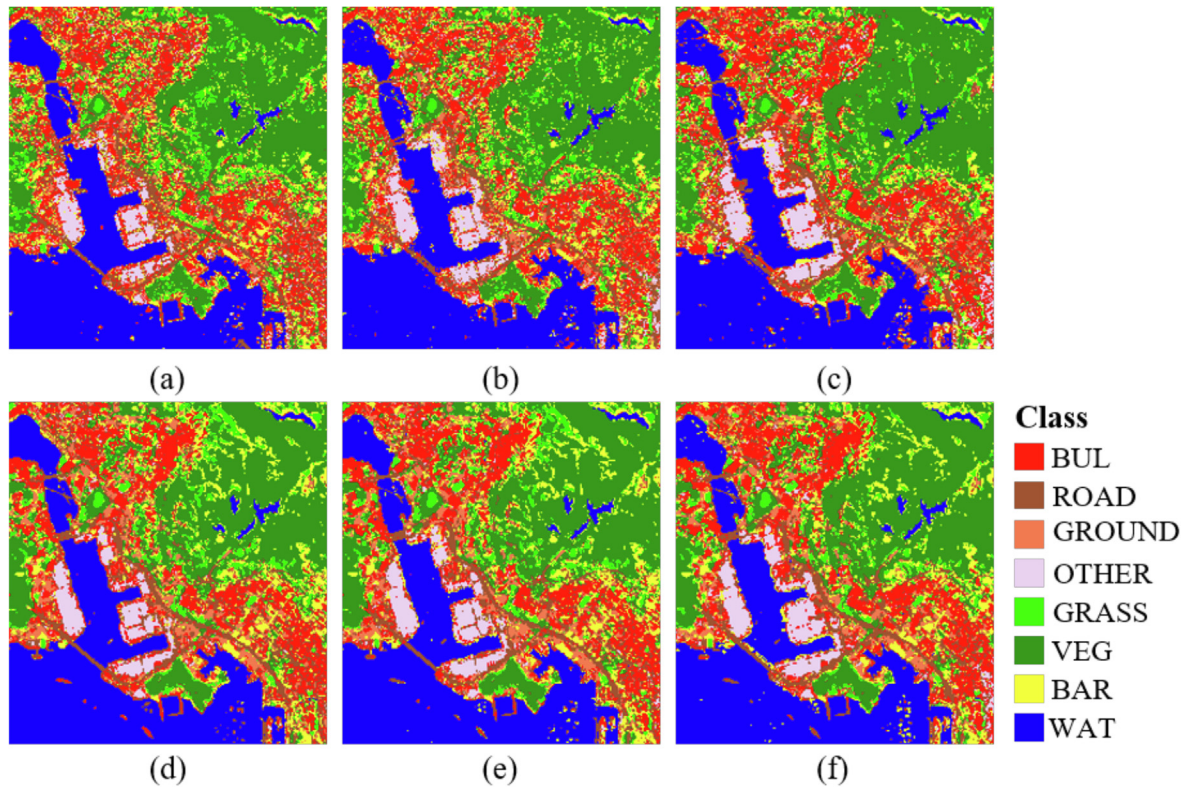
Fig. 8. Classification result of Case 1 using OSSRC. (a). g-L8. (b). g-L8-S1. (c). g-L8-ALOS2. (d). g-GF5. (e). g-GF5-S1. (f). g-GF5-ALOS2.
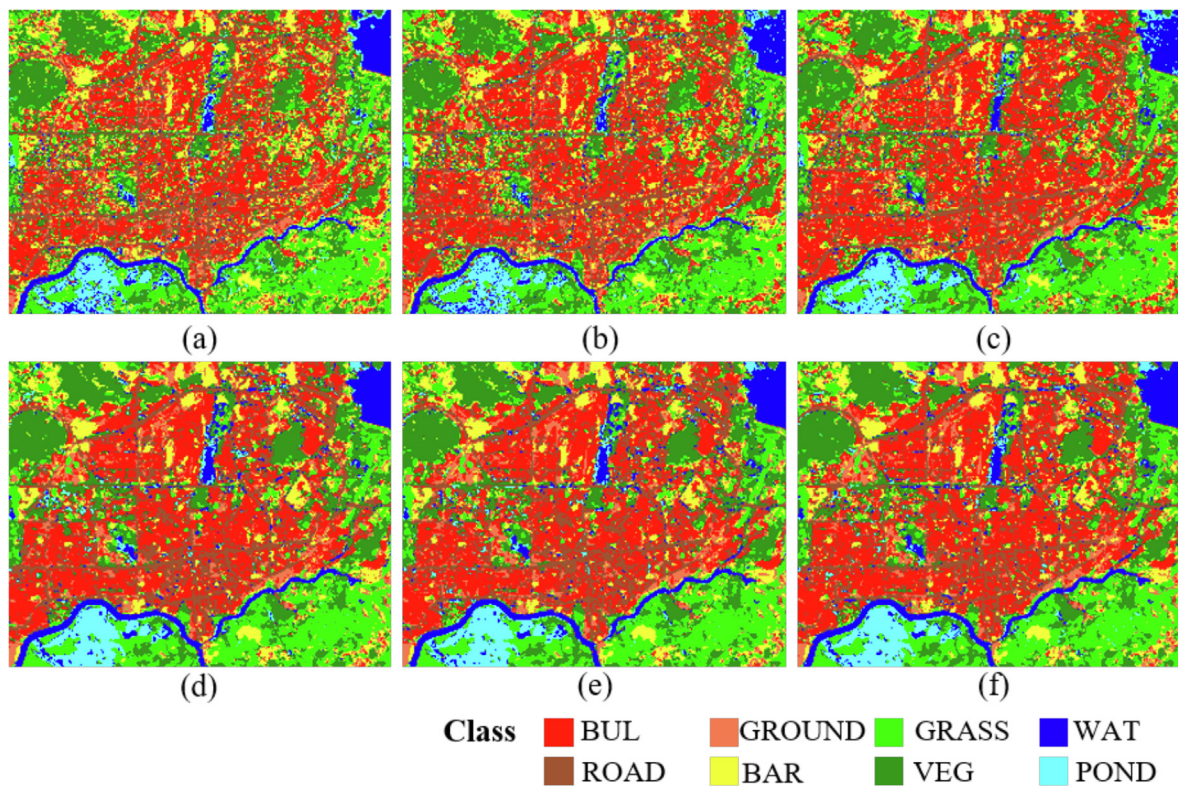

Fig. 9. Classification result of Case 2 using OSSRC. (a). g-L8. (b). g-L8-S1. (c). g-L8-ALOS2. (d). g-GF5. (e). g-GF5-S1. (f). g-GF5-ALOS2.
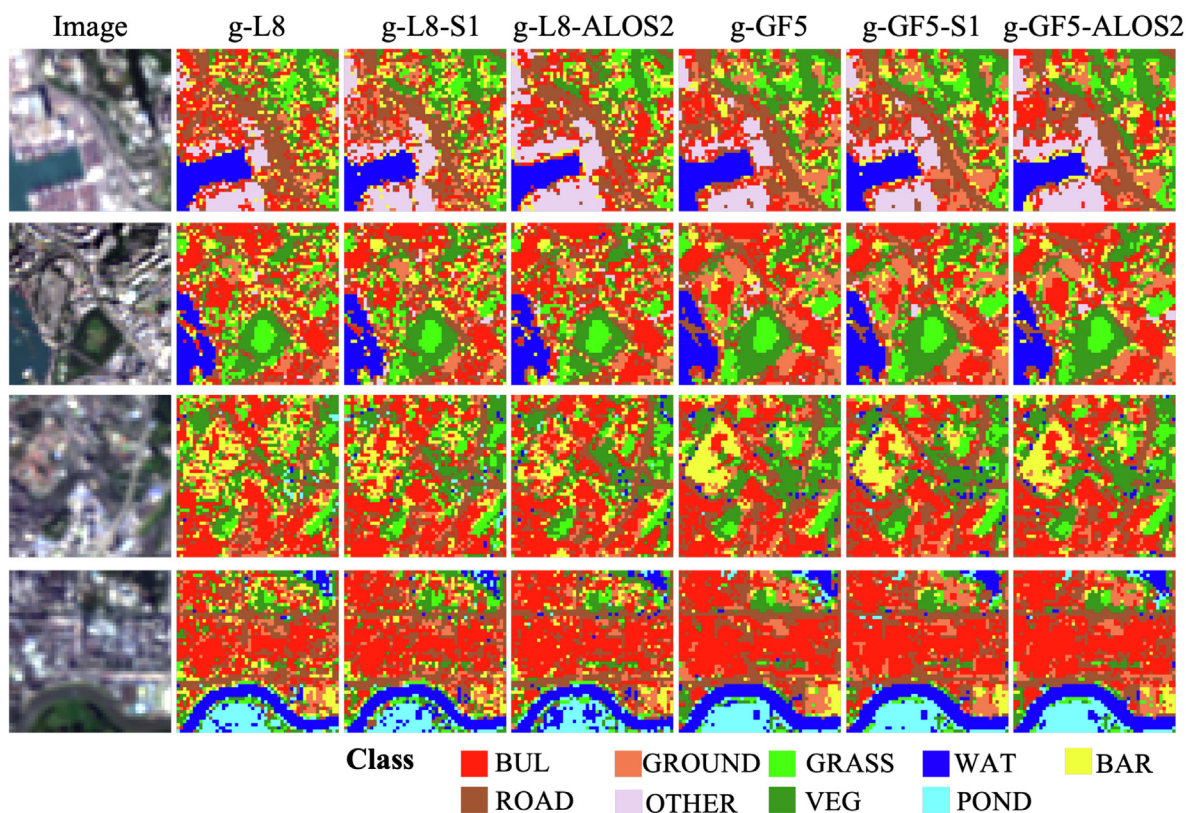
Fig. 10. Classification comparison among different groups.

Table 4
Confusion matrix of GF-5 groups using OSSRC in Case 1.

| GF5-ALOS2 | Ground Truth | | | | | | | | |
Class	BAR	BUL	GRASS	GROUND	OTHER	ROAD	VEG	WAT	Total
BAR	232	9	10	7	1	4	1	0	264
BUL	7	320	0	6	1	19	0	0	353
GRASS	4	1	169	2	0	2	1	0	179
GROUND	7	7	1	130	0	15	1	0	161
OTHER	0	1	0	0	162	0	0	0	163
ROAD	11	24	4	21	5	351	5	0	421
VEG	0	0	3	1	0	3	188	0	195
WAT	0	0	0	0	0	0	0	201	201
Total	261	362	187	167	169	394	196	201	1937
GF5-S1	**Ground Truth**								
Class	BAR	BUL	GRASS	GROUND	OTHER	ROAD	VEG	WAT	Total
BAR	229	7	13	6	2	6	1	0	264
BUL	9	308	1	10	3	22	0	0	353
GRASS	6	2	169	0	0	0	2	0	179
GROUND	8	10	2	123	1	15	2	0	161
OTHER	0	0	0	0	163	0	0	0	163
ROAD	18	23	3	14	1	356	6	0	421
VEG	0	0	4	0	0	3	188	0	195
WAT	0	0	0	0	0	0	0	201	201
Total	270	350	192	153	170	402	199	201	1937
GF5	**Ground Truth**								
Class	BAR	BUL	GRASS	GROUND	OTHER	ROAD	VEG	WAT	Total
BAR	228	7	11	6	2	8	2	0	264
BUL	9	314	1	8	1	20	0	0	353
GRASS	6	3	166	1	0	1	2	0	179
GROUND	8	6	5	126	0	15	1	0	161
OTHER	0	0	0	0	163	0	0	0	163
ROAD	15	19	2	18	2	356	9	0	421
VEG	0	0	6	0	0	2	187	0	195
WAT	0	0	0	0	0	0	0	201	201
Total	266	349	191	159	168	402	201	201	1937

Y. Lin, H. Zhang, G. Li et al.

Egypt. J. Remote Sensing Space Sci. 25 (2022) 1045–1056

Table 5
Confusion matrix of Landsat 8 groups using OSSRC in Case 1.

L8-ALOS2	Ground Truth								
Class	BAR	BUL	GRASS	GROUND	OTHER	ROAD	VEG	WAT	Total
BAR	196	10	16	16	2	16	8	0	264
BUL	17	276	0	21	6	33	0	0	353
GRASS	13	1	152	0	0	6	7	0	179
GROUND	22	22	1	77	0	36	3	0	161
OTHER	0	2	0	0	157	4	0	0	163
ROAD	15	51	9	25	11	298	12	0	421
VEG	2	0	9	3	0	3	178	0	195
WAT	0	0	0	0	0	1	0	200	201
Total	265	362	187	142	176	397	208	200	1937
L8-S1	**Ground Truth**								
Class	BAR	BUL	GRASS	GROUND	OTHER	ROAD	VEG	WAT	Total
BAR	174	25	20	12	5	17	10	1	264
BUL	21	222	0	28	8	72	2	0	353
GRASS	13	1	146	3	0	6	10	0	179
GROUND	18	35	6	65	3	32	2	0	161
OTHER	2	5	0	1	148	7	0	0	163
ROAD	18	65	9	31	11	278	6	3	421
VEG	5	4	13	2	0	0	171	0	195
WAT	0	0	0	0	0	2	0	199	201
Total	251	357	194	142	175	414	201	203	1937
L8	**Ground Truth**								
Class	BAR	BUL	GRASS	GROUND	OTHER	ROAD	VEG	WAT	Total
BAR	182	19	20	7	4	25	7	0	264
BUL	26	225	1	26	11	62	2	0	353
GRASS	13	0	146	6	0	5	9	0	179
GROUND	17	21	7	78	3	33	2	0	161
OTHER	5	9	0	3	136	10	0	0	163
ROAD	23	60	11	40	8	268	11	0	421
VEG	4	2	10	2	0	7	170	0	195
WAT	0	0	0	0	0	0	0	201	201
Total	270	336	195	162	162	410	201	201	1937

Table 6
Friedman significant test for different groups in diagonal symmetry. (S1: Sentinel-1, L8: Landsat 8).

p	GF5-ALOS2	GF5-S1	GF5	L8-ALOS2	L8-S1	L8
GF5-ALOS2	–	–	0.0002***	–	–	–
GF5-S1	–	–	0.0462*	–	–	–
GF5	0.0002***	0.0462*	–	–	–	4.15E-23***
L8-ALOS2	–	–	–	–	–	2.16E-17***
L8-S1	–	–	–	–	–	0.0002***
L8	–	–	4.15E-23***	2.16E-17***	0.0002***	–

SAR polarization backscattering coefficient also contributed to intra/inter-class discrimination. The improvements for multispectral data were higher than hyperspectral data. The result showed that the linear classifier with g-GF5-ALOS2 performed the best in terms of the accuracy and the computation time. Compared with two SAR features, the high dimension spectral features outweighed the results. Still, the VV/VH polarization demonstrated its advantages. VV backscattering intensity was higher in the building areas than the road, which can help the sub-class UIS discrimination.

6. Conclusion

We statistically quantified the contribution of synergizing hyperspectral and polarimetric features to UIS extraction. Hyperspectral and SAR polarization features significantly improve the UIS mapping to reduce inter-class (UIS and bare land) and intra-class (sub-class UIS, e.g., building and road) confusions. Overall, the PolSAR improvement in multispectral data is higher than in the hyperspectral data. In multispectral data, both full and dual PolSAR improve the UIS extraction and the improvements from full PolSAR are much larger than dual PolSAR. In hyperspectral data, the improvements from full PolSAR are significant while it is not so significant from dual PolSAR, the results of which may be the unbalanced feature dimension from optical and SAR data. Specifically, OSSRC outperforms SVM, RF and FCNN in hyperspectral data and full PolSAR combination, which is applicable for fine UIS extraction. The proposed integration of hyperspectral and PolSAR data will improve the accuracy of UIS monitoring and environmental analysis.

Declaration of Competing Interest

The authors declare that they have no known competing financial interests or personal relationships that could have appeared to influence the work reported in this paper.

Acknowledgments

Y. Lin, H. Zhang, G. Li et al.

Egypt. J. Remote Sensing Space Sci. 25 (2022) 1045–1056

References

Al-Wassai, Firouz A, and NV Kalyankar. 2013. "Major limitations of satellite images." *arXiv preprint arXiv:1307.2434.*

Breiman, L., 2001. Random forests. Mach. Learn. 45 (1), 5–32.

Cao, J., Hao, J., Lai, X., Vong, C.-M., Luo, M., 2016. Ensemble extreme learning machine and sparse representation classification. J. Franklin Institute 353 (17), 4526–4541.

Cristianini, N., Shawe-Taylor, J. (Eds.), 2000. An Introduction to Support Vector Machines and Other Kernel-based Learning Methods. Cambridge University Press.

Demsar, J., 2006. Statistical comparisons of classifiers over multiple data sets. J. Mach. Learn. Res. 7, 1–30.

Efron, B., Hastie, T., Johnstone, I., Tibshirani, R., 2004. Least angle regression. Ann. Stat. 32 (2), 407–499.

Fitzgerald, R.W., Lees, B.G., 1994. Assessing the classification accuracy of multisource remote-sensing data. Remote Sens. Environ. 47 (3), 362–368.

Gamba, P., Dell'Acqua, F., 2003. Increased accuracy multiband urban classification using a neuro-fuzzy classifier. Int. J. Remote Sens. 24 (4), 827–834.

Glorot, X., Bengio, Y., 2010. Understanding the difficulty of training deep feedforward neural networks. Paper Presented at the Proceedings of the Thirteenth International Conference on Artificial Intelligence and Statistics.

Guo, H.D., Yang, H.N., Sun, Z.C., Li, X.W., Wang, C.Z., 2014. Synergistic use of optical and polSAR imagery for urban impervious surface estimation. Photogramm. Eng. Remote Sens. 80 (1), 91–102. https://doi.org/10.14358/Pers.80.1.91.

He, K., Zhang, X., Ren, S., Sun, J., 2015. Delving deep into rectifiers: Surpassing human-level performance on imagenet classification. Paper Presented at the Proceedings of the IEEE International Conference on Computer Vision.

Hochberg, J., Tamhane., A., 1987. Multiple Comparison Procedures. John Wiley & Sons, In..

Hu, J.L., Hong, D.F., Wang, Y.Y., Zhu, X.X., 2019. A comparative review of manifold learning techniques for hyperspectral and polarimetric SAR image fusion. Remote Sens. (Basel) 11 (6), 681.

Hu, X.F., Weng, Q.H., 2011. Impervious surface area extraction from IKONOS imagery using an object-based fuzzy method. Geocarto Int. 26 (1), 3–20.

Jiang, L.M., Liao, M.S., Lin, H., Yang, L.M., 2009. Synergistic use of optical and InSAR data for urban impervious surface mapping: A case study in Hong Kong. Int. J. Remote Sens. 30 (11), 2781–2796.

Li, X., Shen, H., Li, H., Zhang, L., 2016. Patch matching-based multitemporal group sparse representation for the missing information reconstruction of remote-sensing images. IEEE J. Sel. Top. Appl. Earth Obs. Remote Sens. 9 (8), 3629–3641.

Lin, Y., Zhang, H., Li, G., Wang, T., Wan, L., Lin, H., 2019. Improving impervious surface extraction with shadow-based sparse representation from optical, SAR, and LiDAR data. IEEE J. Sel. Top. Appl. Earth Obs. Remote Sens. 12 (7), 2417–2428.

Lin, Y., Zhang, H., Lin, H., Gamba, P.E., Liu, X., 2020. Incorporating synthetic aperture radar and optical images to investigate the annual dynamics of anthropogenic impervious surface at large scale. Remote Sens. Environ. 242, 111757.

Lin, Y., Zhang, H., Ma, P., Lin, H., 2020. A shadow free multisource stack sparse autoencoder framework for urban impervious surface mapping. Paper Presented at the IGARSS 2020–2020 IEEE International Geoscience and Remote Sensing Symposium.

Ling, J., Zhang, H., Lin, Y., 2021. Improving urban land cover classification in cloud-prone areas with polarimetric SAR images. Remote Sens. (Basel) 13 (22), 4708.

Liu, Y.-N., Zhang, J., Zhang, Y., Sun, W.-W., Jiao, L.-L., Sun, D.-X., Hu, X.-N., Ye, X., Li, Y.-D., Liu, S.-F., Cao, K.-Q., Chai, M.-Y., Zhou, W.-Y.-N., 2019. The advanced hyperspectral imager: Aboard China's GaoFen-5 satellite. IEEE Geosci. Remote Sens. Mag. 7 (4), 23–32.

Lu, D.S., Hetrick, S., Moran, E., 2011. Impervious surface mapping with Quickbird imagery. Int. J. Remote Sens. 32 (9), 2519–2533.

Lu, D.S., Weng, Q.H., 2009. Extraction of urban impervious surfaces from an IKONOS image. Int. J. Remote Sens. 30 (5), 1297–1311.

Mairal, Julien, F Bach, J Ponce, G Sapiro, R Jenatton, and G Obozinski. 2014. "Spams: A sparse modeling software, v2. 3." *URL http://spams-devel. gforge. inria. fr/downloads. html.*

McCoy, R.M., 2005. Field methods in remote sensing. Guilford Press.

Mercier, A., Betbeder, J., Rumiano, F., Baudry, J., Gond, V., Blanc, L., Bourgoin, C., Cornu, G., Ciudad, C., Marchamalo, M., Poccard-Chapuis, R., Hubert-Moy, L., 2019. Evaluation of Sentinel-1 and 2 Time Series for Land Cover Classification of Forest-Agriculture Mosaics in Temperate and Tropical Landscapes. Remote Sens. (Basel) 11 (8), 979.

Ratha, D., Gamba, P., Bhattacharya, A., Frery, A.C., 2020. Novel techniques for built-up area extraction from polarimetric SAR images. IEEE Geosci. Remote Sens. Lett. 17 (1), 177–181.

Shao, Z.F., Fu, H.Y., Fu, P., Yin, L., 2016. Mapping urban impervious surface by fusing optical and SAR data at the decision level. Remote Sens. (Basel) 8 (11), 945.

Shokrollahi, M., Ebadi, H., 2016. Improving the accuracy of land cover classification using fusion of polarimetric SAR and hyperspectral images. J. Indian Soc. Remote Sens. 44 (6), 1017–1024.

Small, D., 2011. Flattening gamma: Radiometric terrain correction for SAR imagery. IEEE Transactions on Geoscience and Remote Sensing 49 (8), 3081–3093. In press.

Steinhausen, M.J., Wagner, P.D., Narasimhan, B., Waske, B., 2018. Combining Sentinel-1 and Sentinel-2 data for improved land use and land cover mapping of monsoon regions. Int. J. Appl. Earth Obs. Geoinf. 73, 595–604.

Sukawattanavijit, C., Chen, J., Zhang, H., 2017. GA-SVM algorithm for improving land-cover classification using SAR and optical remote sensing data. IEEE Geosci. Remote Sens. Lett. 14 (3), 284–288.

Sun, G.Y., Kong, Y.N., Jia, X.P., Zhang, A.Z., Rong, J., Ma, H.Z., 2019. Synergistic use of optical and dual-polarized SAR data with multiple kernel learning for urban impervious surface mapping. IEEE J. Sel. Top. Appl. Earth Obs. Remote Sens. 12 (1), 223–236.

Sun, Z.C., Xu, R., Du, W.J., Wang, L., Lu, D.S., 2019. High-resolution urban land mapping in china from sentinel 1A/2 imagery based on google earth engine. Remote Sens. (Basel) 11 (7), 752.

Tachikawa, T., Kaku, M., Iwasaki, A., Gesch, D.B., Oimoen, M.J., Zhang, Z., Danielson, J. J., Krieger, T., Curtis, B., Haase, J., 2011. ASTER Global Digital Elevation Model Version 2-Summary of Validation Results. NASA.

Tang, F., Xu, H.Q., 2017. Impervious surface information extraction based on hyperspectral remote sensing imagery. Remote Sens. (Basel) 9 (6), 550.

Veci, L., Prats-Iraola, P., Scheiber, R., Collard, F., Fomferra, N., Engdahl, M., 2014. The sentinel-1 toolbox. Proceedings of the IEEE International Geoscience and Remote Sensing Symposium (IGARSS).

Wan, L., Lin, Y., Zhang, H., Wang, F., Liu, M., Lin, H., 2020. GF-5 hyperspectral data for species mapping of mangrove in Mai Po, Hong Kong. Remote Sens. (Basel) 12 (4), 656.

Weng, Q.H., 2012. Remote sensing of impervious surfaces in the urban areas: Requirements, methods, and trends. Remote Sens. Environ. 117, 34–49. https://doi.org/10.1016/j.rse.2011.02.030.

Weng, Q.H., Hu, X.F., Lu, D.S., 2008. Extracting impervious surfaces from medium spatial resolution multispectral and hyperspectral imagery: a comparison. Int. J. Remote Sens. 29 (11), 3209–3232.

Wright, J., Yang, A.Y., Ganesh, A., Sastry, S.S., Ma, Y., 2009. Robust face recognition via sparse representation. IEEE Trans. Pattern Anal. Mach. Intell. 31 (2), 210–227.

Wu, C.S., Murray, A.T., 2003. Estimating impervious surface distribution by spectral mixture analysis. Remote Sens. Environ. 84 (4), 493–505.

Xu, X., Li, J., Li, S.T., Plaza, A., 2019. Subpixel Component Analysis for Hyperspectral Image Classification. IEEE Trans. Geosci. Remote Sens. 57 (8), 5564–5579.

Yang, J., He, Y.H., 2017. Automated mapping of impervious surfaces in urban and suburban areas: Linear spectral unmixing of high spatial resolution imagery. Int. J. Appl. Earth Obs. Geoinf. 54, 53–64.

Yuan, F., Guo, H., Xu, H., Li, W., Luo, S., Lin, H., Yuan, Y., 2010. China's first special economic zone: The case of Shenzhen. *Building engines for growth and competitiveness in China.* The World Bank.

Zhang, Y.S., Jiang, X.W., Wang, X.X., Cai, Z.H., 2019. Spectral-Spatial Hyperspectral Image Classification with Superpixel Pattern and Extreme Learning Machine. Remote Sens. (Basel) 11 (17), 1983.

Zhang, H.S., Lin, H., Wang, Y.P., 2018. A new scheme for urban impervious surface classification from SAR images. ISPRS J. Photogramm. Remote Sens. 139, 103–118. https://doi.org/10.1016/j.isprsjprs.2018.03.007.

Zhang, H., Ru, X.u., 2018. Exploring the optimal integration levels between SAR and optical data for better urban land cover mapping in the Pearl River Delta. Int. J. Appl. Earth Obs. Geoinf. 64, 87–95.

Zhang, H., Wan, L., Wang, T., Lin, Y., Lin, H., Zheng, Z., 2019. Impervious surface estimation from optical and polarimetric SAR data using small-patched deep convolutional networks: A comparative study. IEEE J. Sel. Top. Appl. Earth Obs. Remote Sens. 12 (7), 2374–2387.

Zhang, Y., Zhang, H., Lin, H., 2014. Improving the impervious surface estimation with combined use of optical and SAR remote sensing images. Remote Sens. Environ. 141, 155–167. https://doi.org/10.1016/j.rse.2013.10.028.